

Mantle flow under the western United States from shear wave splitting

Thorsten W. Becker ^{a,*}, Vera Schulte-Pelkum ^b, Donna K. Blackman ^c,
James B. Kellogg ^d, Richard J. O'Connell ^e

^a Department of Earth Sciences, University of Southern California, Los Angeles, California, USA

^b CIRES, Department of Geological Sciences, Boulder, Colorado, USA

^c IGPP, Scripps Institution of Oceanography, University of California, San Diego, La Jolla, California, USA

^d University of California, Santa Barbara, California, USA

^e Harvard University, Cambridge Massachusetts, USA

Received 12 November 2005; received in revised form 3 May 2006; accepted 3 May 2006

Available online 16 June 2006

Editor: R.D. van der Hilst

Abstract

We show that *SKS* splitting in the westernmost United States (polarization of the fastest shear waves and splitting times, including their back-azimuthal dependence) can be explained by a geodynamic model that includes a continuum-mechanics description of plate motions and underlying asthenospheric circulation. Models that include a counterflow at depths of ~ 300 km are preferred, which may indicate a far-field effect of the Farallon slab anomaly sinking underneath the central continental United States. This finding is broadly consistent with earlier suggestions, and we demonstrate that a mechanically coupled system, though with a strong viscosity contrast with depth, is consistent with the data. We explore the depth dependence of predicted anisotropy by means of computing seismogram synthetics and comparing synthetic splits with observations. Some patterns in the data, including null observations, are matched well. Linked models of geodynamic flow and mineral alignment in the mantle provide a means to test the relationship between strain and the saturation of texturing. Lower fabric saturation strains than for global models are preferred by the data, which may reflect the relatively active tectonic setting and thin asthenosphere of the study region. In general, our results show that seismic anisotropy, when interpreted jointly with mineral physics theories, may be used to quantitatively constrain the spatial character of flow, and the degree of force coupling, at depth.

© 2006 Elsevier B.V. All rights reserved.

Keywords: seismic anisotropy; mantle convection; western US tectonics; shear wave splitting

1. Introduction

Parts of the upper mantle are seismically anisotropic and particularly shear wave splitting from *SKS* waves has often been used to infer deformation and flow at

depth [1,2]. Especially in continental regions such studies may be used to constrain the degree of lithosphere-mantle coupling [3,4], an issue that is still debated. We wish to contribute to this discussion and test if a geodynamic model of mantle flow and inferred lattice preferred orientation (LPO) of olivine can explain the observed anisotropy. We focus on splitting observations in the westernmost United States (Fig. 1), for

* Corresponding author.

E-mail address: twb@usc.edu (T.W. Becker).

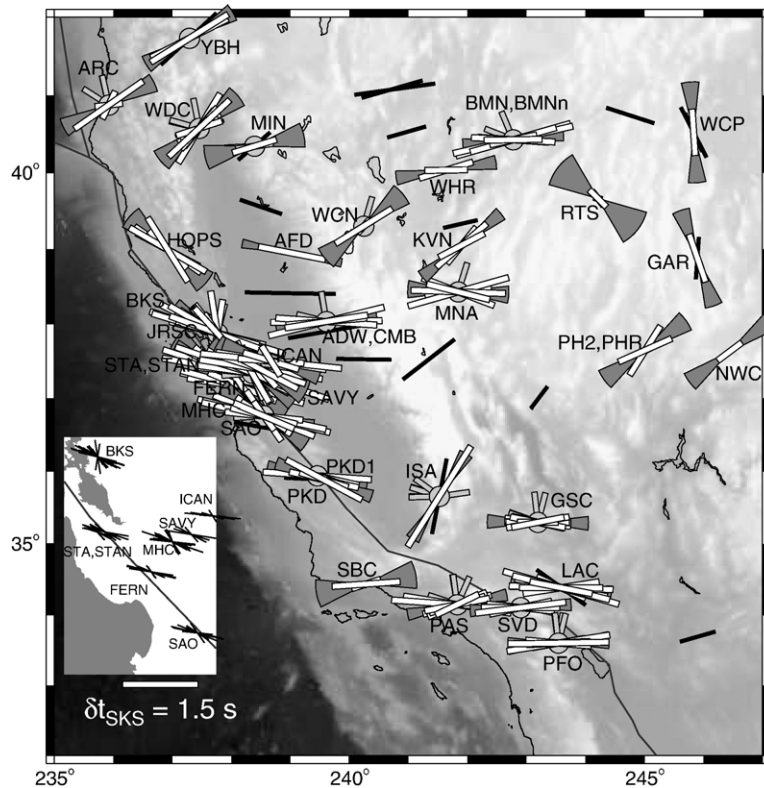


Fig. 1. SKS splitting measurements, station codes, topography, and simplified plate boundary geometry for our study region. Individual splits with available event information from [6,9] as used for misfit evaluation are plotted with white bars, denoting fast azimuths while stick length scales with delay time (see legend). Dark gray wedges show the average fast azimuth uncertainty for each station, oriented with the mean azimuth (constant length). Light gray circles indicate null measurements with small stick showing the event back-azimuths for these nulls. Black sticks on main map are data from the ASU compilation [11] and include work from [12], for which we were not able to obtain event information. Black sticks on northern California zoom show selected data on different scale.

several reasons: the data coverage there is better than in geologically more simple regions such as oceanic plates and can be expected to improve significantly through the EarthScope program. For a continental region, the setting is relatively simple as the region is tectonically young and underlain by slow velocity anomalies, indicating a thin lithosphere [e.g. [5]]. Lastly, previous interpretations of the data have invoked a variation of the polarization orientation of the fastest shear wave (fast azimuth) with depth from parallel to the San Andreas Fault in the shallow mantle [6–8] to close to E–W deeper [6,9,10]. The splitting signal along the San Andreas has recently also been compared with the tectonic setting in New Zealand using a model that includes lateral viscosity contrasts in the lithosphere across the plate boundary [4].

Of particular interest here is the model by Silver and Holt [13] (hereafter: SH02), who used surface strain-rates from geodesy and SKS splitting to infer an EW oriented return flow underneath North America

(in a hotspot reference frame), whereas the surface motion of the plate is NESW (in both hotspot and no-net-rotation reference frames). In the kinematic description chosen by SH02, a complete decoupling of the lithosphere from the underlying asthenospheric flow is suggested. Here, we substantiate our earlier findings that an alternative model with a continuum mechanics treatment of plate motion and underlying mantle flow fits the data just as well for typical radial viscosity profiles, though with a low viscosity, asthenospheric channel [14]. We use a global circulation model similar to Becker et al. [15], with recent improvements due to inclusion of the Kaminski and Ribe [16] method of predicting LPO development and treatment of lateral variations in viscosity [17,18], though we do not fully explore the latter at this point. To generate synthetic splitting that is as close as possible to the published seismological results, we improve on Hall et al.'s [19] and Fouch et al.'s [48] studies and compute full waveforms. We show that

not only fast azimuths but also the amplitudes of delay times can be explained by mantle-based LPO anisotropy, allowing inferences on the accumulated finite strain. A large degree of waveform complexity is predicted, which casts doubt on simple interpretations of anisotropy as being due to one or two layers with hexagonal symmetry in the horizontal plane. Models that include density anomalies due to geodynamic subduction models [20,21] lead to reduced misfits compared to those based on plate-motion driven flow only, or based on density inferred from global shear wave tomography. We find that the inferred density structure of the mantle appears to have the strongest effect on anisotropy predictions and flow, compared to other uncertainties such as lateral viscosity variations. It may thus be possible to use anisotropy for tests of models of the tectonophysical history of the region [*cf.* [22]].

2. Data

Fig. 1 shows available shear wave splitting data for the study region, and the subset selected for our study from [6,9]. Moving east from the Pacific to the North American plate, fast propagation directions trend roughly NW–SE and turn in the plate boundary region to a more W–E orientation. Data from different studies agree overall on regional scales, but there are large variations in splitting at individual stations depending on event back-azimuth. Such variations require a departure from the simplest model of a single layer of hexagonal anisotropy with a horizontal fast axis. The existence of plunging symmetry axes [23], orthorhombic symmetry [10], depth-dependent anisotropy [6,9,12], or a combination of the above can therefore be expected in our study region. Published splitting results alone do not, however, provide sufficient constraints to separate the effects above, even if waveforms are taken into account [9,12,10].

Our selected dataset consists of 277 individual, apparent single layer [64] splitting observations from 34 distinct stations, out of which 215 are non-nulls. The average formal uncertainties are $\approx 11^\circ$ and 0.4 s for fast azimuth and delay time estimates, respectively. While there is more splitting data available in principle [12,24], we were not able to reconstruct crucial event-station information needed to compute the back-azimuth for any other study. This highlights the need for a standardized, comprehensive archiving of anisotropy results, and –better– a consistent reanalysis of the anisotropy data, also exploring alternative measures of body wave anisotropy [25].

3. Modeling anisotropy

We are mainly considering sub-lithospheric anisotropy, but recognize the potentially complicating nature of the crust and lithospheric mantle in the sense of carrying frozen-in anisotropy from past tectonics. There may also be brittle damage anisotropy with a more complicated relationship to large-scale viscous deformation than mantle LPO. As we will show, the match of mantle-based LPO predictions to observations is good, implying either coherence of mantle and lithospheric deformation, or a negligible effect of near-surface contamination. We study upper mantle anisotropy which is likely due to LPO alignment of intrinsically anisotropic minerals deforming under dislocation creep [*e.g.* [26,27]]. Such power-law deformation is typically associated with depth regions shallower than ~ 400 km [28], where most anisotropy seems to be residing [29]. The relevance of deeper anisotropy [*e.g.* [30,31]] on general shear wave splitting is not clear at present. Some of the rheological parameters for the upper mantle are also still poorly constrained [32], which makes absolute diffusion and dislocation creep viscosities model parameters, rather than tight constraints [33]. We will therefore assume that LPO forms within the upper ~ 400 km of the mantle, and consider waves accumulating signatures of anisotropy from 375 km depth up to the surface. We experiment with excluding top or bottom layers to evaluate the role of having a much simplified lithospheric deformation model, and possible overestimation of the depths of anisotropy formation, respectively.

4. Mantle flow

Global mantle flow in a spherical shell is estimated based on prescribing plate motions on the surface while the core–mantle boundary is mechanically free-slip [15]. The buoyancy driven component of flow, and lateral viscosity variations for some models, are inferred from seismic velocity anomalies as imaged and inferred from a range of tomography and subduction models, analyzed in detail in [34]. We have verified that the buoyancy forces in such models would lead to realistic plate velocities [35]. The simplest, best-fit model parameters based on our previous work [15] are used, for example a constant density:shear wave velocity anomaly scaling of $d\ln\rho/d\ln v_s = 0.15$. The buoyancy forces due to the imposed density structure of the mantle have a strong effect on the flow, and depth-dependent and compositional effects may be important. Here, we will test the performance of models based on purely

plate-related flow, those including density inferred from tomography, and those where we use only slabs from reconstructions by Lithgow-Bertelloni and Richards [20] (*lrr98d*) and Steinberger [21] (*stb00d*, all models in italics use nomenclature as in [34]). All geodynamic model set-ups are listed in Table 1. By comparing a wide range of models, insight into the general sensitivity of anisotropy to density anomalies can be gained; we leave detailed studies of different, regional tomography models and scalings to temperature for later.

We denote any radial reference viscosity structure we use by η_0 . This viscosity is typically a generic profile suggested by Hager and Clayton [36] which we call η_D , with $\eta_D=50$ (depths $z<100$ km), $\eta_D=0.1$ ($100 \text{ km} \leq z<410$ km), $\eta_D=1$ ($410 \text{ km} \leq z<660$ km), and $\eta_D=50$

for $z \geq 660$ km, in units of 10^{21} Pas. Profiles similar to η_D can be used to fit the geoid and other global constraints; η_D also leads to good global azimuthal anisotropy misfits for surface wave models [15]. We will also consider a more complex profile, η_F , as suggested by Steinberger [37], which has a more tapered transition to higher viscosity in the lower mantle, and a more simple profile, η_C , that lacks the low viscosity channel of η_D and has $\eta_C=1$ for $100 \text{ km} \leq z<660$ km.

The equations for instantaneous, incompressible, infinite Prandtl number flow are solved using the semi-analytical method of Hager and O'Connell [38] for the reference models with only radially varying viscosity. We also employ the 3-D, spherical finite element code CitcomS, slightly modified from [39] as provided by geoframework.org. The procedure is described in more detail in [18], and we will only briefly discuss models with lateral viscosity variations which were inferred using a simplified rheological law:

$$\eta(z, T, \dot{\epsilon}) = B(z) \dot{\epsilon}_{II}^{\frac{1}{n}-1} \eta_0(z) \exp\left[\frac{E}{n}(T_c - T)\right] \quad (1)$$

where η_0 is the radial viscosity profile, T_c is the non-dimensional reference temperature (0.5), $\dot{\epsilon}_{II}$ is the second (shear) strain-rate tensor invariant, E scales the strength of the temperature effect (chosen as 0 or 30), n is the power-law exponent (1 or 3), and B is a constant adjusted for each layer such that the laterally averaged viscosity is roughly equal for radially varying (η ; $\{E=0, n=1\}$), temperature dependent ($\eta(T)$; $\{E=30, n=1\}$), and temperature and strain-rate dependent ($\eta(T, \dot{\epsilon})$; $\{E=30, n=3\}$) cases. Tomographic anomalies are used to infer non-dimensional temperature anomalies as $dT/d\ln v_S = -4.2$, with $E=30$, this leads to lateral viscosity variations of up to approximately two orders of magnitude [18]. We furthermore explicitly limit η to vary only from 10^{17} to 10^{24} Pas, and implicitly constrain $\eta(\dot{\epsilon})$ variations because our imposed strain-rates due to plate motion variations across boundaries are quite small given the moderate numerical resolution we are able to employ.

Most models discussed here, however, are Newtonian $\{E=0, n=1\}$. This is inconsistent with the dislocation creep regime assumption for LPO formation. We find that, regionally, power-law flow is fairly similar to Newtonian flow for our low resolution models [17]. For simplicity, we also use only no-net-rotation (NNR) plate motions, as our initial tests with net plate shear yielded increased misfits between predicted and observed fast azimuth for global surface wave anisotropy [15]. Moreover, we only consider steady-state flow; given the similar orientation of North America's plate

Table 1
Overview of all geodynamic flow models that were considered

Label	Density structure	Viscosity	Surface plate motions
Plate-related flow only			
–		η_D (four layer reference viscosity)	NUVEL [40]
–		η_C (three layer viscosity)	”
–		η_F best-fit viscosity from [37]	”
Slab anomaly models			
	<i>lrr98d</i> [20]	η_D	NUVEL
		η_F	”
	<i>stb00d</i> [21]	η_C	”
		η_D	”
		η_F	”
B1	<i>stb00d</i>	η_D	KHH03 [41]
Tomography models			
B2	<i>vox5p</i> [$d\ln v_F$; [42]]	η_D	NUVEL
	<i>pmean</i> [$d\ln v_P$; [34]]	η_D	”
	<i>ngrand</i> [$d\ln v_S$; [43]]	η_D	”
	<i>smean</i> [$d\ln v_S$; [34]] plus NA00 [$d\ln v_S$; [5]]	η_D	”
	<i>smean</i>	η_C	”
		η_D	”
		η_F	”
		η_D	KHH03
		η_F	”
		η_D plus $\eta(T)$ dependence	NUVEL
		η_D plus $\eta(\dot{\epsilon}, T)$ dependence	”

Density/tomography model abbreviations as in [34] with references given in parentheses. For details about other modeling parameters, see [35,15].

For each velocity model, LPO texture was computed for saturation strains of $\xi_c = 0.5, 1$, and 2. Preferred best-fit model B1 is used for Figs. 3 and 4a–c, and B1 and B2 for $\xi_c = 0.5$ are marked on Figs. 5b and 6.

motion in the study region in hotspot and NNR reference frames, the latter simplification is likely of greater concern [also see discussion in [18]]. Models are thus most applicable to oceanic or young continental regions, where past tectonic episodes may be less important for seismic anisotropy. In the study area, we expect thin lithospheric regions toward the plate boundary to be better modeled than areas further East, as long as fabrics represent mainly recent deformation.

5. LPO fabrics

There is field and laboratory evidence on how the crystallographic axes of olivine, an inherently anisotropic mineral, align with shear [e.g. [44,45]], and mineral physics theories allow quantitative estimates of LPO development [46,16]. Anisotropy has been modeled on regional and global scales [e.g. [47,19,48,13,49,15,50]], and such linked geodynamic and seismic models successfully reproduce part of the observed structure. Recent work has focused on evaluating some of the previous simplifying assumptions such as only radially varying and Newtonian viscosity, or using finite strain ellipsoid (FSE) orientations instead of LPO from fabric computations [17,51]. Becker et al. [18] show that there is an encouraging match between synthetic LPO calculated for mantle flow models and that documented for natural samples. This indicates that kinematic methods for estimating LPO [16] may indeed be applied to nature, which is an assumption under which we shall proceed.

We use the kinematic LPO texturing theory of Kaminski and Ribe [16], hereafter *KR*, in the D-REX implementation [53] (Table 2 lists anisotropy abbreviations used). This method is computationally faster than the VPSC approach [46] and the match to laboratory data for simple deformation regimes is good [54]. Given the low spatial resolution of our flow models, we expect differences between VPSC and *KR* approaches to be small [55,56], but this has not yet been evaluated explicitly for our flow models. Details of the implementation are described in [18], and we only list the key ingredients here. We assume dominance of low water/stress, “classic”, A-type [in the nomenclature of [45]] slip systems throughout the upper 410 km of the mantle since fabrics such as B-type may be restricted to limited geographic regions [57]. All parameters for the *KR* method are chosen as in [53], meaning that we are attempting to account for dynamic recrystallization, grain boundary migration, and are generally using a 70% olivine (ol)/30% enstatite (en) mineral assemblage of ~2000 virtual grains per sample.

Table 2
Anisotropy abbreviations used

Abbreviation	Meaning
FSE	Finite strain ellipsoid. The principal axis ratios of the FSE measure the degree of total strain as expressed by ξ and ζ .
LPO	Lattice preferred orientation of intrinsically anisotropic olivine crystals leading to deformation-induced seismic anisotropy.
ISA	Infinite strain axis: the largest FSE axes if a velocity gradient would apply for infinite times in steady-state flow, exists only for small vorticity [52].
KR	Kaminski and Ribe [16] kinematic method of predicting LPO from velocity gradients along streamlines.
SC	Single crystal (elasticity tensor, as a function of pressure and temperature), as opposed to the Voigt averaged assemble of LP oriented olivine grains.
TI	Fast symmetry axis of a best-fit hexagonal tensor derived from an assemblage tensor as predicted from LPO fabrics and single crystal elastic moduli measurements.

Following [15,18], we advect tracers in flow and let LPO develop along the path until the logarithmic saturation strain, ξ_c , defined as the maximum of

$$\xi = \log(e_1/e_2) \text{ and } \zeta = \log(e_2/e_3), \quad (2)$$

has reached a critical value of $\xi_c \sim 0.5\text{--}2$. Here, e_1, e_2, e_3 are the largest, intermediate, and smallest eigenvalue of the FSE, respectively. Tracers arrive with random LPO from below 410 km depth, as the phase transition there is likely to erase fabrics. We also employ a maximum advection time of 60 Ma, to not over-stretch the assumption of stationary flow.

The concept of using a saturation strain stems from Ribe’s [58] earlier theory of LPO development, where he showed that a finite strain of $\xi_c \sim 0.5$ is sufficient to overprint any preexisting fabric. If more recent laboratory results are taken into account, the saturation behavior is more complicated [52]. We have conducted experiments on what ξ values are needed to reorient existing LPO fabrics [18] and found that $\xi_c \sim 1\text{--}2$ generally suffices to overprint LPO patterns after a change in deformation regimes.

Kaminski and Ribe [52] suggested using the Infinite Strain Axis (ISA) as a proxy for LPO fabrics, as the ISA tends to align with the orientation of the LPO-predicted fast *P*-wave propagation direction. For steady-state flow, the ISA is defined at each point by the orientation of the largest FSE axis that would develop if the velocity gradient at this location were to apply for infinite times. The ISA only exists if the vorticity is small [$|T| \leq 1$ in the notation of [52]], else both LPO and ISA keep

spinning indefinitely. If the ISA exists, the rate at which LPO fabrics conform to that axis is measured by the Grain Orientation Lag [II , eq. (7) of [52]]. If $II \gg 1$, the LPO will be strongly dependent on the deformation history; if $II \ll 1$, LPO will form quickly and align with the ISA.

We have explored using the ISA axes of [52] instead of LPO predictions. Within our study region, mantle flow typically exhibits quite large rotational components, locally with $\Gamma > 1$ at depths between ~ 150 and 250 km. We could thus not compute the ISA in $\sim 50\%$ of the study region. Moreover, the ISA itself does not contain any information about the symmetry class or the amplitudes of seismic anisotropy. These complications limit the usefulness of the ISA for our modeling work. Where the ISA was defined, it typically aligned with the best-fit hexagonal (TI) axis as predicted from the LPO we compute following the ξ_c streamlines. This confirms the validity of our approach. The alignment between ISA and TI was better for models with larger saturation strains of $\xi_c \sim 1-2$, compared to $\xi_c \sim 0.5$ cases, though not by much. In regions of mismatch between ISA and TI, II values are typically large, indicating that deformation-history dependent development of LPOs needs to be considered instead of the ISA. While computationally far less demanding, the ISAs can thus not be used to predict anisotropy at all locations in our flow model where we wish to evaluate it for wave propagation. We therefore chose to use the strain saturation approach where the full fabric LPO is computed along a streamline using a finite strain cut-off criterion according to ξ_c for advection. Using ξ_c involves uncertainties about the degree of saturation of LPO, particularly at small strains. However, those uncertainties can ultimately only be resolved with time-dependent flow computations, which are outside the scope of this paper.

At every desired location where anisotropy is to be predicted, we compute a Voigt-averaged elasticity tensor, C , for the grain assemblage using single crystal (SC) elasticity tensors. The SC tensors for olivine and enstatite (orthopyroxene) as well as their dependence on temperature, T , and pressure, p , (only linear derivatives) were taken from [59]. A 1-D temperature and pressure profile is assumed for C so that p , T change only as a function of depth, and so modify the SC tensors before averaging at each tracer location. The thermal depth profile is (simplified) from [60], and p (without crustal layer) from PREM [61]. We use the full tensor for computing waveforms, and compute best-fitting, hexagonal axes for visualization purposes following [62]. When quoting anisotropy strength for hexagonal

anisotropy, we are referring to tensor norms, which are approximately twice the seismic velocity anomalies. The uncertainties associated with the choices for SC tensors and averaging are discussed in detail in [18]; their effect on hexagonal axis orientation is minor, but may be of order 20% for anisotropy amplitudes.

6. SKS splitting

It is well known that fast azimuths of shear wave splitting measurements depend on back-azimuth for single layers whose anisotropy is not purely hexagonal with axis oriented in the horizontal, and splitting measurements suffer from non-linear superposition effects if anisotropy varies spatially [63,64,65]. However, such important geometries are rarely taken into account for geodynamic interpretation. Hall et al. [19] and Fouch et al. [48] perhaps achieved the greatest seismological realism so far by using superposition of individual 10 km layer splits. This approach may be invalid because of frequency dependent effects [63], but was deemed sufficiently accurate for the specific setting [19]. Here, we employ full waveform modeling that incorporates finite frequency effects, though we do not compute 3-D synthetics, as justified below.

For a single homogeneous layer, one may compute fast orientations and delay times of shear wave splitting by solving the Christoffel equation for arbitrary anisotropy C , at a given phase velocity and ray incidence, e.g. 5° for typical SKS arrivals [e.g. [65]]. When analyzing our flow models, we compute single anisotropy layers for testing purposes by averaging the upper 375 km, where tensors are spaced at 25 km depth intervals. These simplified estimates are compared with a layer matrix computation that accounts for the full depth dependence and waveform complexities. We follow the formulation by Kennett [66] with anisotropic extensions [67,68]. The harmonic response of a horizontal layer stack to an incident plane wave is summed over a range of frequencies (0–5 Hz) to obtain a pulse seismogram (i.e. a series of δ -functions) via inverse Fourier transform.

Then we apply bandpass filters from 0.05 to 0.3 Hz to construct synthetic seismograms in the SKS band (~ 7 s period). This method is equivalent to a reflectivity formulation, except that we do not integrate over slowness, since SKS is well approximated as plane waves with a single slowness, and slowness is preserved in anisotropic horizontally layered media. The horizontal layers can have general anisotropy, including plunging symmetry axes, and we vary the back-azimuth of the incoming plane S waves.

We use a cross-correlation method [69,70] to determine splitting from modeled waveforms. In the noise-free, single-splitting case, this method is equivalent to the popular method of Silver and Chan [71]; however, in the presence of complex anisotropy with multiple splits per waveform, results may vary significantly between the two methods [69] and the cross-correlation method may be more robust overall [72]. We mostly use the implementation by Menke and Levin [70] to compute splitting measurements but also tested other, related approaches [69] and found that results were, expectedly, very similar. For the individual station results, we also estimate a “splitting complexity” factor as a function of back-azimuth based on the performance of the standard, single layer splitting measurement techniques. This factor indicates how well a single anisotropic layer can explain the seismograms as computed from our geodynamic model. A single-layer split produces identically shaped fast and slow pulses. Splitting complexity, κ , is computed from the maximum correlation, or unity minus the minimum norm of the rotated seismogram traces from the best-fit cross-convolution [R_{\min} parameter of [70]] and falls between zero (perfect data reduction) and unity (failure of single layer cross-convolution method). Ideally, identical splitting measurement techniques should be applied to observed and modeled waveforms. Since we are using several observational studies with variations in the splitting measurement method used, we try to match the synthetics splitting method to that used in each observational study as closely as possible. While likely of second order compared to uncertainties in geodynamic modeling parameters, possible biases should be kept in mind.

To evaluate model performance quantitatively, we compare real and synthetic splitting measurements and compute the angular deviation of fast azimuths, $\Delta\alpha$ ($0 \leq \Delta\alpha \leq 90^\circ$, with $\langle \Delta\alpha \rangle = 45^\circ$ the random mean), and the delay time misfit $\Delta\delta = \delta_{\text{model}} - \delta_{\text{data}}$ ($\Delta\delta > 0$ indicating over-prediction of anisotropy). The misfit is evaluated for each station by two methods. First, we use all misfits for each individual, back-azimuth dependent splitting measurement. Second, we also compute the misfit between mean estimates where both measurements and synthetics α and δ are first averaged over all back-azimuths. For every flow model, we then compute weighted means of $\Delta\alpha$ and $\Delta\delta$, $\langle \Delta\alpha \rangle$ and $\langle \Delta\delta \rangle$, where each misfit is weighted by the inverse of the product of formal splitting measurement uncertainties of the data (σ^α and σ^δ respectively), and the splitting complexity, κ , as computed from the cross-convolution measurements.

If subscript i denotes the i -th splitting measurement out of N , then

$$\langle \Delta\alpha \rangle = \frac{1}{W^\alpha} \sum_{i=1}^N \frac{1}{\kappa_i \sigma_i^\alpha} \alpha_i \quad \text{and} \quad \langle \Delta\delta \rangle = \frac{1}{W^\delta} \sum_{i=1}^N \frac{1}{\kappa_i \sigma_i^\delta} \Delta\delta_i. \quad (3)$$

Here, W^α and W^δ are normalization factors so that the weights (e.g. $1/(\kappa_i \sigma_i^\delta)$) sum up to unity. In this way, we put more emphasis on those synthetics where a researcher would have most likely identified a good, single layer splitting signal. We do not consider any measurements with $\delta_{\text{data}} < 0.2$ s (including nulls) for the mean misfits. Our choice of using $\langle \Delta\delta \rangle$ may yield misleadingly low misfits for models that strongly over-predict δ for some, but underpredict other stations, though this is typically not the case. Ranking model performance using the L^2 norm, $|\Delta\delta|$, leads to very similar results than using average $\Delta\delta$ values as in Eq. (3). The same holds true if we discard the formal splitting uncertainties and use no weighting for $\langle \Delta\alpha \rangle$ ($\langle \Delta\alpha \rangle = 1/N \sum \alpha_i$); most models rank similarly regardless of the formal misfit criterion. Below, we discuss other possible ways of judging misfits besides computing average values such as $\langle \Delta\alpha \rangle$ and $\langle \Delta\delta \rangle$.

Should variations in anisotropy be shorter wavelength than the Fresnel zone, the layered approach fails and finite frequency effects need to be considered, either by full waveform modeling [e.g. [73]] or by using sensitivity kernels [74]. Using Chevrot’s [75] method, we have tested if kernel based estimates of splitting intensity [25] were different for full 3-D media rather than constant anisotropy layers. Differences for typical sites were found to be small; we conclude that the layer matrix seismograms are appropriate for our models, though higher resolution models may require further evaluation.

Since we assume that LPO fabrics do not affect mantle rheology to make the problem more tractable, the complete particle tracking, KR, and seismogram computation step can be done by post-processing. The software package to do this can be obtained from <http://geodynamics.usc.edu/~becker/>.

7. Results

Fig. 2 compares modeled velocities at different layers with predicted fast seismic azimuth, as visualized by hexagonal axes, at depth. (We only show TI axes for reference, the full tensor is used for the seismological modeling below.) For this particular region and flow

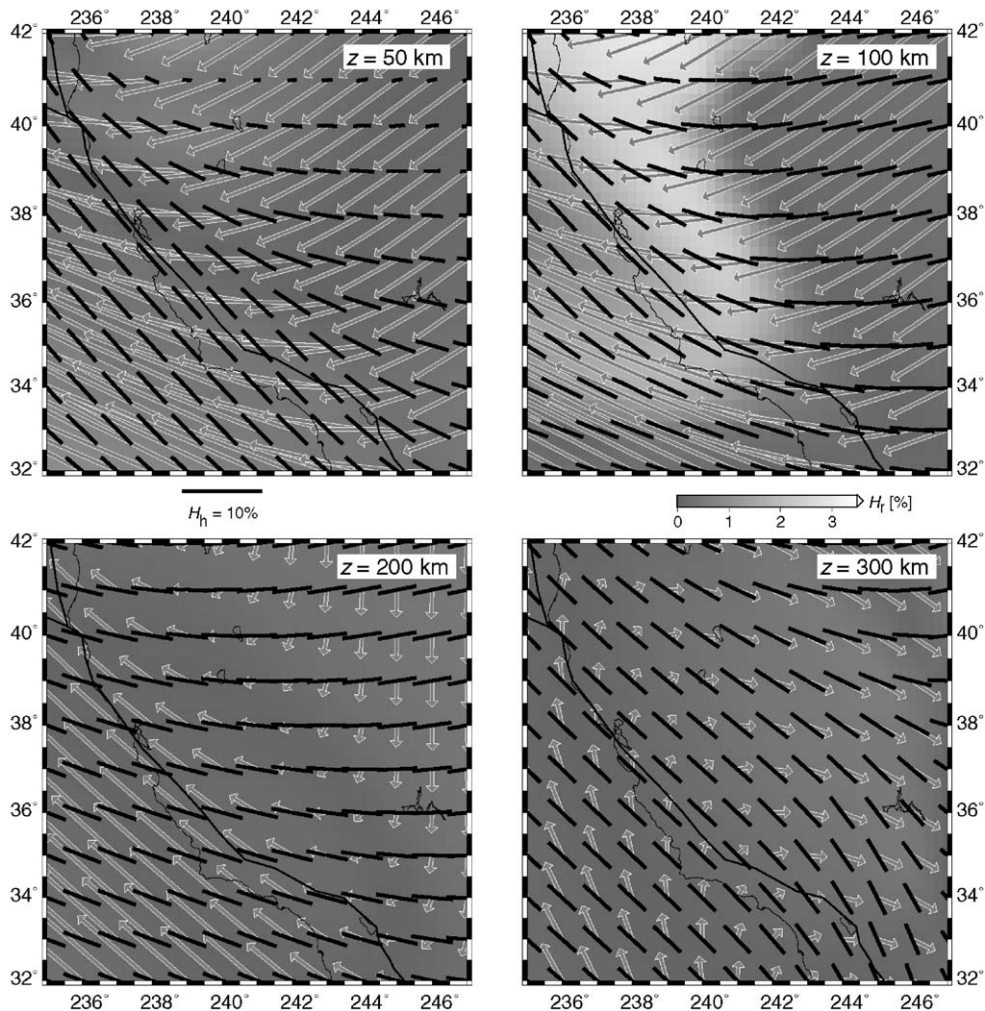


Fig. 2. Flow velocities in a no-net-rotation reference frame (open vectors; maximum varies from ~ 5 , top, to ~ 1 cm/yr, bottom layer) and best-fit hexagonal anisotropy (TI) axes from KR fabrics based on flow computations (black sticks: horizontal projection, background shading: radial component). Scales for the horizontal and radial TI components, H_h and H_r , respectively are given in the middle of the plot in anisotropy tensor norm fractions. The preferred geodynamic model is shown at four different depth levels and based on *stb00d* slabs, η_D , advection strains of $\xi_c=1$, and surface velocities from [41].

model at $\xi_c=1$, the depth averaged mean anisotropy is 7.6% for tensor norms. Out of this, the hexagonal symmetry component makes up $\sim 79\%$ [cf. [62,18]], the largest remainder, $\sim 17\%$ of the total, is orthorhombic. The strength of the orthorhombic component is sufficient to cause significant back-azimuthal variation in a single layer with a horizontal symmetry axis when incidence angles are $10\text{--}15^\circ$ (*SKKS*). However, for the steep *SKS* incidence angle of 5° modeled here, back-azimuthal variations will be small even for stronger orthorhombic symmetry. Therefore, the main cause for variation with back-azimuth will be a plunge of the symmetry axis or layering. The background shading in Fig. 2 denotes the radial component of the best-fit

hexagonal anisotropy, the anisotropy is mostly horizontal in general. RMS variations of the plunge axis for the study region are generally below $\sim 10^\circ$ out of the horizontal, though locally plunge angles of $\sim 45^\circ$ are reached.

Given our model resolution and the steady-state flow assumption, the best-fit hexagonal axes will roughly align with both the FSE (for typical straining amounts) and flow vectors at depth for most regions [52,18]. Correspondingly, the predicted pattern of mantle flow at depth is similar to the fast azimuth orientations in many, but not all, regions (Fig. 2). From the shallow layer to 100 km depth, we notice a smooth transition between North American and Pacific plate motion, whereas

strain accumulation, and hence anisotropy formation is relatively slow within the North American (high viscosity) lithosphere at 50 km depth. If we consider only plate-related motion, and no buoyancy effects by means of up or downwellings, this smoothed plate motion transition pattern continues to larger depths of ~ 400 km. However, if we include large scale flow due to the down-going Farallon slab as in Fig. 2, such as in *stb00d* (the main slab anomaly is off to the north-west at depths of ~ 450 km), the pattern at depth is changed to more E–W oriented fast azimuths in the center of the study region near the plate boundary, at ~ 200 km depth. At larger depths, fast axes rotate clockwise to NW–SE orientations. Similar rotations and even stronger non-horizontal components of hexagonal anisotropy throughout the upper ~ 300 km are found in many of our models (shading in Fig. 2, in this model radial components mostly limited to depths $\lesssim 150$ km). This leads us to expect complex back-azimuth dependence in shear wave splitting.

In our computations, shallow ($\lesssim 50$ km) deformation and resulting LPO is dominated by the prescribed plate motions which are surface boundary conditions. Typically, we use rigid plate models such as NUVEL–NNR [40], and velocity transitions between plates are smoothed out by the spherical harmonic parameterization we employ for consistency across all computations. We take vector field expansions up to spherical harmonic degree $\ell_{\max}=63$ and taper high harmonics with a \cos^2 filter to suppress ringing. Alternatively, we can directly incorporate the plate boundary deformation at the present-day by using models such as Kreemer et al. [41] (hereafter: KHH03) which includes intraplate deformation as seen by GPS geodesy. We discuss below that well fitting models are not very sensitive to these two alternative surface boundary conditions, but our best-fitting slab model (as shown in Fig. 2) includes intraplate deformation, as did SH02. Hexagonal orientations for the same model shown in Fig. 2 but using rigid plate velocities, instead of geodetic models, show less strong (but similarly oriented) anisotropy underneath the North American plate at 50 km, more pronounced radial hexagonal components underneath the Pacific Northwest, but display similar patterns at larger depths.

If tomography is used as a density model [e.g., *smean*; [34]], the transition from NE–SW fast azimuths at 100 km to E–W at 200 km is similar to the one depicted in Fig. 2 for the slab model. In contrast to Fig. 2, hexagonal axes rotate back counter-clockwise to NE–SW orientation at larger depths. This effect is due to currents at ~ 400 km depth from a slow anomaly

upwelling underneath the Pacific plate with local maximum SW of the Juan de Fuca plate, not included in the slab-density model used for Fig. 2. This upwelling ties into a larger scale pattern of flow northward from the southern Pacific which turns E and SE underneath North America once it interacts with the Farallon anomaly. The latter is more strongly imaged in *P* wave tomography than in *S* wave models [e.g. 34], and the EW currents seen for the slab model in Fig. 2 are more pronounced.

Besides the density model, another factor in determining the flow and anisotropy pattern is the radial viscosity structure. For the slab model in Fig. 2, the hexagonal axes orientations are quite robust with regard to η , e.g. when η_C or η_F are used instead of η_D . However, for *smean* tomography, the deeper layers at ~ 300 km depth are strongly dependent on the viscosity layering, as η_C without a low viscosity channel leads to dominance of plate motion patterns at larger depths, compared to η_D and η_F that allow different kinds of shear flows to develop. The drop in viscosity of profiles such as η_D allows rotation of flow with depth, while it still causes strong force transmission between the lithosphere and the deep mantle on a global scale [35]. Differences between models are emphasized if we compare models with larger ξ_c strain accumulation, as expected. We explore the dependency of anisotropy on ξ_c below.

Fig. 3 shows synthetics and observed splits for our preferred, best-fit model with *stb00d* slab-density structure, $\xi_c=0.5$, KHH03 surface velocities, η_D , and LPO from depth ranges 75 km to 350 km (model B1 of Table 1). All well performing models show similar features as the one depicted in Fig. 3, and we discuss sensitivities below. In agreement with our earlier, simpler models [14], we find that the shear wave splitting pattern is well matched. While a comparison with SH02's decoupling model has to remain visual, the agreement seems as good, or better than SH02. This implies that both physical models, a simplified, layered approach with presumably weak force transmission between plate and mantle [13], and our continuum-mechanics descriptions of plate and mantle flow [e.g. [35]], may be invoked to explain the splitting signal.

With the exception of station ISA at the southern end of the Great Valley, many of the observations that are not well matched by our model are found in the north-west or in the Basin and Range. Local misfits such as station WCP or GAR may be affected by small-scale flow patterns which are not incorporated in our flow model, or lateral differences in the rigidity of geologic units. For instance, a shallow plume has been

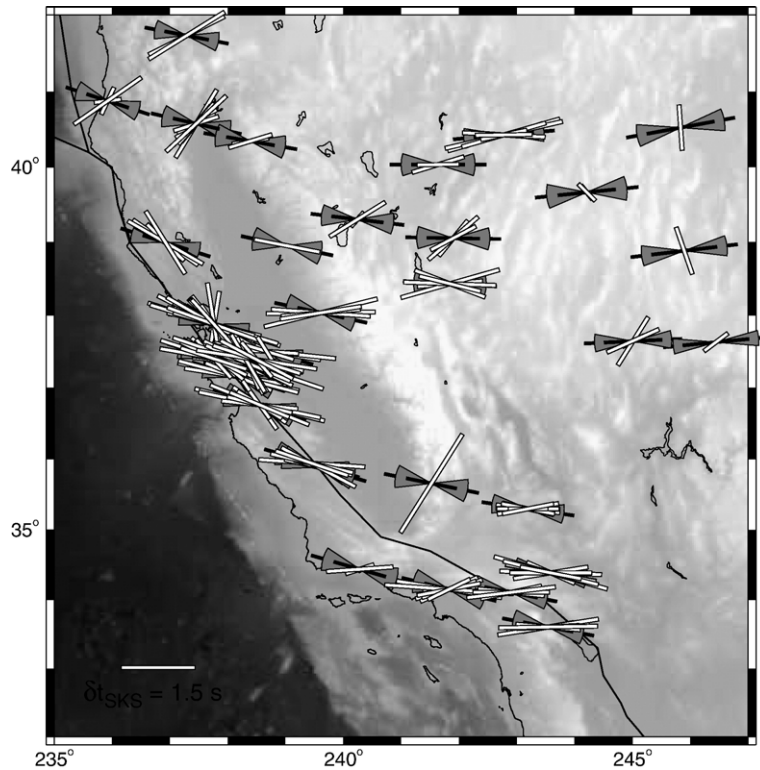


Fig. 3. Comparison of splitting from observations (white bars, see Fig. 1) and synthetics (gray symbols) for the preferred, best-fitting flow model with *stb00d* slab density, η_D , and KHH03 surface velocities (B1 of Table 1). The strain computation is taken up to $\xi_c=0.5$ and the top 75 km LPO layers have been omitted from the wave propagation simulation. We use a propagator matrix approach and compute splitting for all back-azimuths [70]. The dark gray wedge symbols show the mean and standard deviation, σ_α , based on a full 0–360° scan of fast azimuths of the synthetics, while the black sticks indicate the corresponding variation in delay time ($\pm\sigma_\delta$). For mean misfit computations, we use $\Delta\alpha$ between the individual splits according to their back-azimuth.

suggested to affect anisotropy in the Basin and Range [76].

In the NW, the subducting Juan de Fuca plate may be expected to lead to complications in the flow pattern that are not well captured by our low resolution circulation model. In the Basin and Range, our splitting estimates are both at a 90° angle to measurements and show much larger delay times. One possible interpretation would be that *SKS* splitting senses past deformation and stretching of the older lithosphere, and/or regional flow in the eastern regions of our study area [77]. SH02 chose to focus only on the westernmost observations [as defined by slow tomographic anomalies in the NA00 version of [5]] given that those tectonically active regions may be expected to sense asthenospheric flow more closely. We shall use all available data for model evaluation instead, but emphasize that there are good reasons why our geodynamic model may fail in certain localities. If we exclude stations in the Basin and Range (BMN, RTS, WCP, GAR, PHR, and NWC), $\langle\Delta\alpha\rangle$ misfits are reduced by a small amount $\sim 1\text{--}2^\circ$ but the model ranking in

terms of overall misfits is similar to when those stations are included.

The finding that both SH02 and our approach may be invoked to explain seismic anisotropy may seem like a frustrating confirmation of the non-uniqueness of the *SKS* data [10]. However, with the establishment of the necessary geodynamic and seismological tools, we can readily incorporate other anisotropy datasets, and we can also perform further quantitative tests of synthetic anisotropy models. Fig. 4a)–c) compares synthetics from the preferred B1 model in Fig. 3 for three example stations with a large number of observed splits. To mimic a typical *SKS* splitting measurement, we use a single-layer measurement technique of cross-correlating radial and transverse pulses [70]. As expected from the variations of hexagonal axes with depth in our flow model (Fig. 2), there is a strong dependence of apparent fast propagation plane and delay time on back-azimuth, as the fast hexagonal orientations are neither purely horizontal nor vertically coherent. Even if we average the LPO structure with depth (dashed lines in Fig. 4),

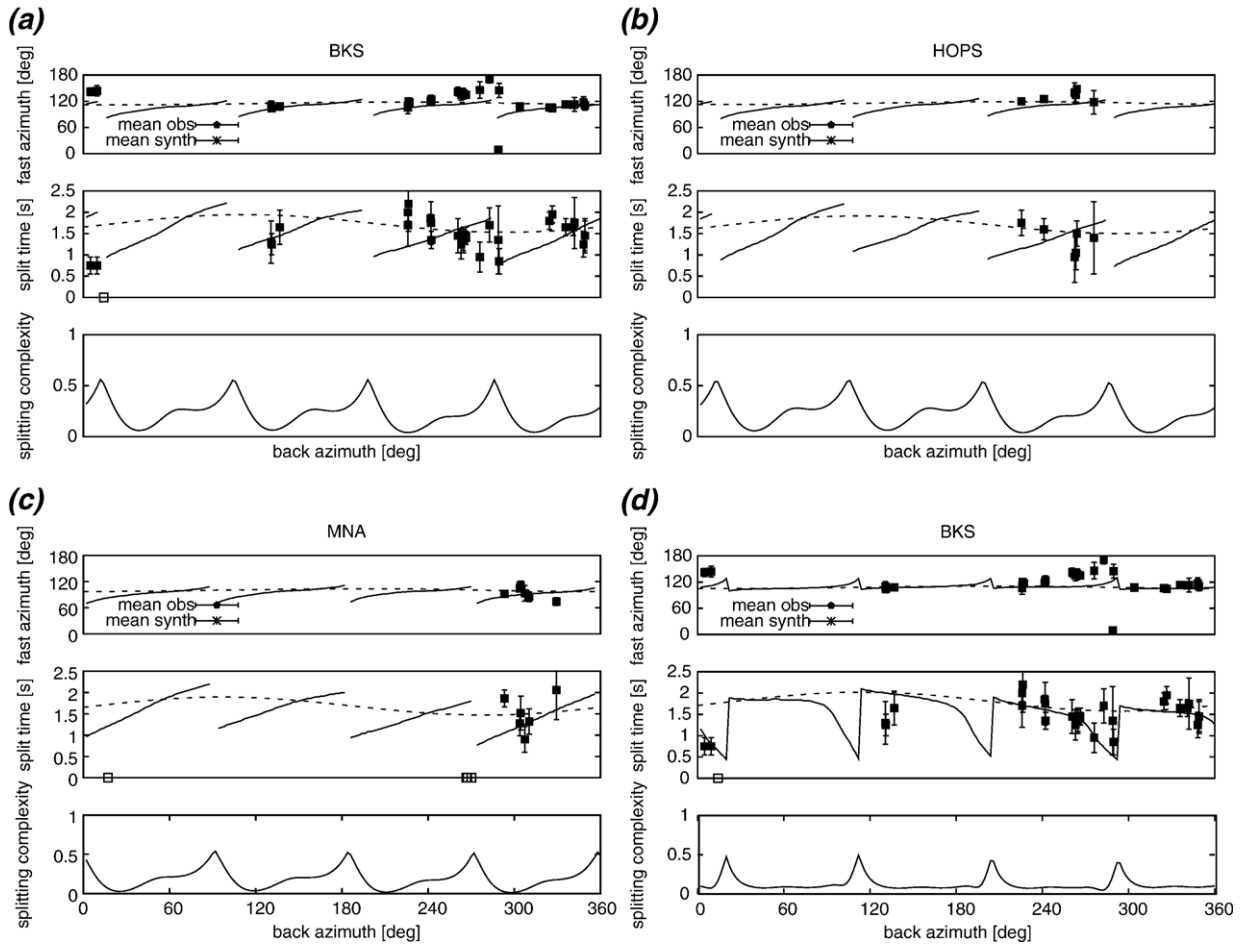


Fig. 4. Comparison of measured splitting (black squares for non-nulls, open square for nulls; see Fig. 1) and synthetics for the preferred geodynamic model shown in Fig. 3 (B1 of Table 1) for three selected stations (a–c). Solid and dashed lines in fast azimuth (top) and delay time (middle) plots are for a full seismogram synthetic using the layered LPO predictions and a splitting measurement [70], and for an average layer of same thickness using the Christoffel approach, respectively. Lower subplots denote the adequacy of a single layer, hexagonal anisotropy model with horizontal symmetry axis (“splitting complexity”) as computed from the rotated seismogram misfit of the cross-convolution method [R_{\min} parameter of 70]. Plot (d) shows station results for BKS using a geodynamic model without any density anomalies and only plate motion related flow. The formal misfit is larger than for the best-fit model used for plots a)–c), but trends such as in δ are matched better visually.

delay times show variations with back-azimuth, though they are not as pronounced.

As a reflection of the complex anisotropic structure, the splitting complexity (κ , performance of the cross-correlation method) is quite large for certain incidences, as split pulses from different depth layers will non-linearly interfere with each other, rendering an interpretation as a single layer misleading. The shape of the κ -function depends on the station location and, more so, the geodynamic model assumptions with regard to density and viscosity structure. We found that many of the null observations in the data lie within regions where the cross-convolution misfit for the synthetics based on this geodynamic model is

high. This is most clearly the case for WDC, GSC, and MNA (around 270° back-azimuth in Fig. 4c), while others nulls (e.g. at PFO) cannot be explained with the same model. This indicates that anisotropy variations with depth as predicted from the geodynamic model may be invoked to explain complications in the splitting data at certain stations.

For the non-nulls, almost all of the measurements for the stations in Fig. 4a)–c) can be fit to within the uncertainties of the data, both with regard to fast azimuth and delay times. Within the limited back-azimuth coverage of the data, the geodynamic model appears to capture some of the observed trends, and in particular the layered model does a better job than the

averaged, Christoffel approach (solid and dashed lines in Fig. 4a–c). However, the misfit is larger for other stations, and visual inspection indicates that layered splitting trends are not everywhere preferred over average layer estimates.

While our best-fit model B1 with subduction-related density anomalies and viscosity structure η_D as shown in Figs. 3 and 4a)–c) has the lowest formal misfit, there are some trends in the fast azimuths and delay times that appear poorly matched, such as around $\sim 250^\circ$ back-azimuth for station BKS (Fig. 4a). We have experimented with several types of formal misfit measures, and always arrived at similar rankings between regional model performance. However, manual inspection of station misfit plots reveals that other classes of models lead to better visual matches of back-azimuth trends, or individual station misfits. One example is shown in Fig. 4d for BKS, where the geodynamic model is similar to the one used for Fig. 4a but does not include density anomalies; flow is driven by plate motions only. Restricted to BKS, the misfits of this plate motion only model are $\langle \Delta\alpha \rangle = 14.5^\circ$ and $\langle \Delta\delta \rangle = 1.6$ s, compared to $\langle \Delta\alpha \rangle = 9.8^\circ$ and $\langle \Delta\delta \rangle = 1.8$ s for the best-fit model in Fig. 4a.

Overall trends of the observed splitting with back-azimuth might be more robust for comparison with geodynamic models for certain stations, but they are also harder to quantify. Our forward modeling experiments indicate that the phase of observed π -periodic back-azimuthal splitting patterns is relatively robustly related to fast axis orientations, while the trends within the pattern are very sensitive to changes in the strength of anisotropy. A possible approach would be to model back-azimuthal patterns observed at stations such as BKS in Monte Carlo style using a few layers by first matching the phase, then the trends, and matching the results to flow models that reproduce the required orientations and strengths as a function of depth. This alternative approach will be subject of a separate paper.

8. Discussion

Fig. 5 shows model performance in terms of $\langle \Delta\alpha \rangle$ and $\langle \Delta\delta \rangle$ for all experiments performed (see Table 1), separated by saturation target strains ξ_c and assumptions on the depth extent of LPO anisotropy. For a “good” model, we will consider low $\Delta\alpha$ and $\Delta\delta$ as criteria, but discuss those separately. A wide range of models with different assumptions on density or viscosity structures are able to fit the data quite well. We show results where all the computed LPO upper mantle anisotropy is used

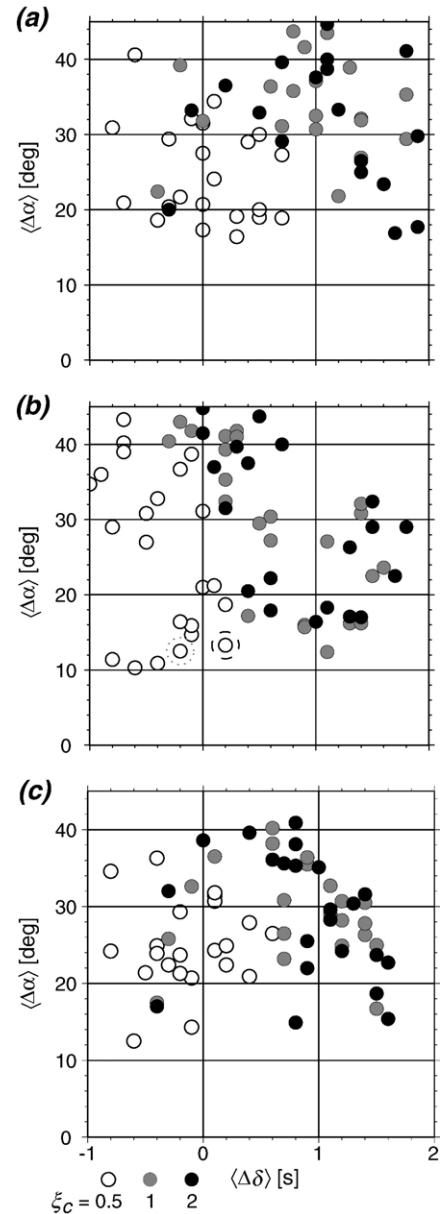


Fig. 5. Model performance (each dot represents a single model) for all experiments of Table 1. The whole upper 375 km of predicted LPO anisotropy is used for (a), and the upper 75 km (b) and everything below 300 km (c) is assumed isotropic, respectively. Measures $\langle \Delta\delta \rangle$ and $\langle \Delta\alpha \rangle$ denote the weighted mean misfits in delay times and fast azimuths, respectively, based on computing synthetic splitting for each event-station pair. White, gray, and black circles denote models with saturation strains of $\xi_c = 0.5, 1,$ and $2,$ respectively. Dotted and dashed circles for plot (b) mark preferred, best-fitting slab (B1) and tomography models (B2), respectively.

above 375 km, and for models where the upper or lower 75 km were assumed isotropic. These models are an attempt to test the effect of unrealistic treatment of the crust and lithospheric mantle, and potential uncertainties

about the depth extent of dislocation creep and LPO formation [78], respectively.

We evaluated if using smoother transitions between North America as in KHH03 consistently lead to better results than using “rigid plate” models such as [40] when incorporated as spherical harmonics. For some models that show poor misfits when using rigid plates, incorporating plate boundary deformation led to large misfit improvements of $\sim 10^\circ$ for $\langle \Delta\alpha \rangle$. However, the effect for better performing models was inconsistent. While our preferred B1 slab model as in Fig. 3 uses KHH03 velocities, there are also well performing models with rigid plates (see below). We therefore leave a detailed study of the influence of the upper ~ 50 km for more appropriate mechanical models that are able to incorporate the lithospheric layer more realistically.

From Fig. 5, we can see that total anisotropy models have best $\Delta\alpha$ values of $\sim 18^\circ$, which can be improved by $\sim 6^\circ$ when removing the top or bottom LPO layers. Removing the top layer most clearly sorts models by delay time misfits following ξ_c , and anisotropy amplitudes are best reproduced for $\xi_c \sim 0.5$. This value is smaller than the required strain of $\xi_c \sim 1.5$ to explain natural sample LPO variations based on flow models [18], while saturation strains were not that sensitive to surface wave anisotropy misfit for FSE models [15]. The finding of preferred smaller ξ_c may reflect the tectonically active character of most of the study region, where we are not capturing changes in local block motions over time. However, we cannot say for sure as the depth extent of power-law and diffusion creep for LPO creation and destruction, respectively, adds uncertainties to anisotropy amplitude interpretations.

Performing a comparison of individual splits for $\langle \Delta\alpha \rangle$ including back-azimuth dependence leads to better mean misfits than using a comparison of station-averaged, mean fast azimuths, by $\sim 5^\circ$ for all models. Though not a dramatic improvement, this reduction in misfit implies that we are partly successful in explaining the back-azimuth variations in the splitting observations using our mantle flow model. If we use a single, average layer for anisotropy and compare the Christoffel method predictions, the misfit is also increased by $\sim 5^\circ$ compared to models with anisotropy variations with depth. While the match for individual stations as shown in Fig. 4 is not convincing as such, these results nonetheless indicate that it is worth while to explore the additional information contained in the splitting measurements beyond simple layer averages. However, further exploration of the

depth dependence and lateral variations of anisotropy will have to await a reanalysis of the waveforms, so as not to be limited by inherent assumptions in the original splitting measurements.

We now limit our considerations mainly to LPO models where the top 75 km LPO was removed, and further evaluate misfits in terms of density model and radial viscosity profile used (Fig. 6). No such comparison can be exhaustive nor lead to unique conclusions, but we can detect certain trends in the part of the model space we explore based on our previous experience with such mantle flow models. In accord with our earlier regional results [14] and global surface wave study [15], we find that flow models that include density-driven flow outperform those with plate-related motions only. Furthermore, slab models such as *lrr98d* and *stb00d* typically lead to reduced model misfits compared to density anomalies based on seismic tomography; performance is comparable for the two slab models. This preference for subduction related flow is also found for complete upper 375 km models (not shown) where a *stb00d* model using η_D at $\xi_c = 0.5$ has misfits of $\langle \Delta\alpha \rangle = 17.3^\circ$; $\langle \Delta\delta \rangle = 0$ s compared to $\langle \Delta\alpha \rangle = 10.3^\circ$; $\langle \Delta\delta \rangle = -0.5$ s for no upper layer models as in Fig. 6. The best slab model in Fig. 6, B1, is also based on *stb00d* and η_D , but employs the KHH03 velocities, rather than rigid plate surface velocity boundary conditions. For this model, $\langle \Delta\alpha \rangle = 12.5^\circ$; $\langle \Delta\delta \rangle = -0.2$ s (B2, marked with dashed circle in Fig. 6 and shown in Fig. 3). These misfits are comparable to the uncertainties in the data.

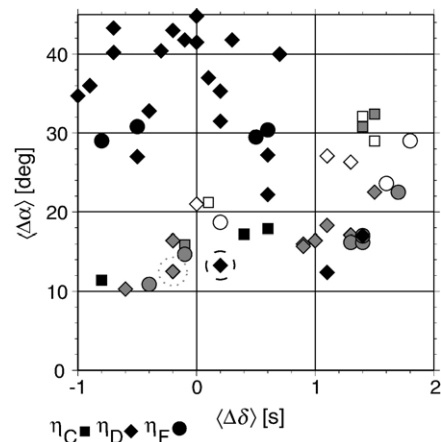


Fig. 6. Model performance for experiments where the upper 75 km of LPO have been removed (as in Fig. 5b), sorted by type of density structure (open boxes: only plate-related flow, gray: tomography models, black: tomography, see Table 1) and radial viscosity profile (only $\{E=0, n=1\}$ cases, see legend). Dotted and dashed circles mark preferred, best-fitting slab (B1) and tomography models (B2), respectively.

Global S wave tomography models such as *smean* often lead to poorer model performance, such as $\langle \Delta\alpha \rangle = 34.7^\circ$, $\langle \Delta\delta \rangle = -1.0$ s for the η_D models which typically lead to good model fits for global anisotropy [15]. However, for the same model and η_C viscosity, the misfit is improved to $\Delta\alpha = 11.4^\circ$, albeit at $\langle \Delta\delta \rangle = -0.8$ s. For P wave tomography, our *pmean* reference model leads to poor performance, but using the *vox5p* [42] and η_D , we measure low misfits of $\langle \Delta\alpha \rangle = 13.3^\circ$; $\langle \Delta\delta \rangle = 0.2$ s (marked by dashed circle in Fig. 6). Overall, the dependence on the radial viscosity profiles is not clear cut, but the lower viscosity asthenosphere in η_D appears to be preferred by the data over η_C , consistent with [15] and a range of earlier geodynamic studies [36]. While we are starting to explore lateral viscosity variations and power-law flow, our initial tests [17] indicate that differences are minor when low resolution, global models are used. Such models are clearly not entirely realistic; however, they may serve to get a first impression of the order of magnitude of effects. For the *stb00d* model, misfits to the *SKS* data are changed from $\langle \Delta\alpha \rangle = 17.3^\circ$ to 16.8° when using $E=30$ “temperature” dependent viscosity. For a *smean* model at $\xi_c=0.5$, the angular misfit is increased from 31.5° for $\{E=0, n=1\}$, 32.1° to $\{E=30, n=1\}$, and 34.4° for $\{E=30, n=3\}$. Our tests indicate that differences in flow fields due to rheological variations on large scales may be smaller than the differences between models with simpler, radial and Newtonian viscosity and different tomographic models. The proper evaluation of power-law flow models in three dimensions to backup our inferences is beyond the scope of this study.

We have also begun to explore using regional tomographic models by augmenting our global reference S model, *smean*, with NA00 [5] surface wave tomography but found that the misfit to splitting observations increased. This may be because of our simplifying assumptions on converting slowness to temperature anomalies [79]. Regional tomography should also be considered to study lithospheric viscosity variations, which may exist between the Pacific and North American and affect the seismic anisotropy [4]. Given the simplified nature of our treatment of lithospheric deformation, we have to postpone further exploration of regionalized structural models. With our limited selection of seismic tomography models, and the numerous simplifying assumptions in our flow model, we interpret our findings on the density structure such that certain P wave models and all slab models available to us exhibit flow patterns that are better able to explain anisotropy than long-wavelength S wave models. Similar return flow at depth has been suggested before

[21,13] and our finding substantiates the existence of such currents and their effects on observables. Rather than arguing that one density model is better than the other, the more general insight is that regional shear wave splitting may indeed be related to flow at depth, and so, by inference, detect density anomalies, *e.g.* due to subducted slabs.

9. Conclusions

Models such as ours indicate that regional seismic anisotropy in the western US is consistent with simplified mantle flow models, substantiating earlier conclusions based on global datasets. Splitting can be explained both in terms of amplitudes and fast azimuths using kinematically based methods for computing the development of LPO during mantle flow [16], where preferred geodynamic models exhibit a return current at depth driven by the Farallon anomaly. This is similar to what was suggested by Silver and Holt [13], yet the physical model is different. Our continuum approach implies that mantle flow couples to the plates, although it is mediated by a drop in viscosity in the asthenosphere. The radial viscosity profile with such a drop allows strong variations in the direction of flow underneath North America, while there is still strong force transmission to the plates on a global scale [35]. The interactions between mantle and lithospheric motions need not be weak to explain splitting, implying potentially strong plate driving forces associated with mantle flow.

There is some indication that the depth dependence of anisotropy is correctly modeled and found in the back-azimuth dependence of splits, though complementary datasets, *e.g.* from surface waves, will be needed to substantiate the evidence. Given the sensitivity to density models, geodynamic interpretation of splitting should be useful in constraining the tectonic history of the region, where different plate reconstructions predict different slab locations [22]. It is intriguing that differences in anisotropy predictions are very strong off-shore of California where OBS deployments could yield important new constraints.

Acknowledgments

This work was inspired by extensive discussions with P. Silver, for which we are grateful. We also thank R.D. van der Hilst, M. Savage, and an anonymous reviewer for their constructive and helpful comments, E. Kaminski for providing D-REX, H. Schmeling for comments, A. McNamara, J. van Hunen, and E. Tan for

the help with Citcom, S. Zhong, L. Moresi, M. Gurnis and others involved in geoframework.org for sharing this code, W. Menke for providing his splitting routines, S. Chevrot for the help with kernel splitting intensity computations, B. Steinberger for discussions, and all authors of tomographic and geodynamic models for open data exchange. We are funded by the NSF grants EAR-0330717 and EAR-0409373, and computation for the work described in this paper was supported by the University of Southern California Center for High Performance Computing and Communications (www.usc.edu/hpcc). Most figures were produced with GMT [80].

References

- [1] P.G. Silver, Seismic anisotropy beneath the continents: probing the depths of geology, *Annu. Rev. Earth Planet. Sci.* 24 (1996) 385–432.
- [2] M.K. Savage, Seismic anisotropy and mantle deformation: what have we learned from shear wave splitting? *Rev. Geophys.* 37 (1999) 65–106.
- [3] W.E. Holt, Correlated crust and mantle strain fields in Tibet, *Geology* 28 (2000) 67–70.
- [4] M.K. Savage, K.M. Fischer, C.E. Hall, Strain modelling, seismic anisotropy and coupling at strike-slip boundaries: applications in New Zealand and the San Andreas fault, in: J. Grocott, B. Tikoff, K.J.W. McCaffrey, G. Taylor (Eds.), *Vertical Coupling and Decoupling in the Lithosphere*, *Geol. Soc. Lond. Spec. Pubs.*, vol. 227, Geological Society of London, London, 2004, pp. 9–40.
- [5] S. van der Lee, G. Nolet, Upper mantle S velocity structure of North America, *J. Geophys. Res.* 102 (1997) 22815–22838.
- [6] S. Özalaybey, M.K. Savage, Shear-wave splitting beneath western United States in relation to plate tectonics, *J. Geophys. Res.* 100 (1995) 18135–18149.
- [7] G.P. Smith, G. Ekström, A global study of P_n anisotropy beneath continents, *J. Geophys. Res.* 104 (1999) 963–980.
- [8] V. Schulte-Pelkum, G. Masters, P.M. Shearer, Upper mantle anisotropy from long-period P polarization, *J. Geophys. Res.* 106 (2001) 21917–21934.
- [9] R. Hartog, S.Y. Schwartz, Depth-dependent mantle anisotropy below the San Andreas fault system: apparent splitting parameters and waveforms, *J. Geophys. Res.* 106 (2001) 4155–4168.
- [10] P.M. Davis, Azimuthal variation in seismic anisotropy of the southern California uppermost mantle, *J. Geophys. Res.* 108 (2003) 2052, doi:10.1029/2001JB000637.
- [11] M. Fouch, Upper mantle anisotropy database. available online, (2004), accessed in 12/2004, <http://geophysics.asu.edu/anisotropy/upper/>.
- [12] J. Polet, H. Kanamori, Anisotropy beneath California: shear wave splitting measurements using a dense broadband array, *Geophys. J. Int.* 149 (2002) 313–327.
- [13] P.G. Silver, W.E. Holt, The mantle flow field beneath Western North America, *Science* 295 (2002) 1054–1057.
- [14] T.W. Becker, *Lithosphere-Mantle Interactions*. PhD thesis, Harvard University, Cambridge MA, (2002). <http://geodynamics.usc.edu/~becker/thesis.tp.times10.pdf>.
- [15] T.W. Becker, J.B. Kellogg, G. Ekström, R.J. O’Connell, Comparison of azimuthal seismic anisotropy from surface waves and finite-strain from global mantle-circulation models, *Geophys. J. Int.* 155 (2003) 696–714.
- [16] É. Kaminski, N.M. Ribe, A kinematic model for for recrystallization and texture development in olivine polycrystals, *Earth Planet. Sci. Lett.* 189 (2001) 253–267.
- [17] T.W. Becker, D.K. Blackman, V. Schulte-Pelkum, Seismic anisotropy in the western US as a testbed for advancing combined models of upper mantle geodynamics and texturing (abstract), *EOS Trans. AGU* 85 (47) (2004) T33A–T1338A.
- [18] T.W. Becker, S. Chevrot, V. Schulte-Pelkum, D.K. Blackman, Statistical properties of seismic anisotropy predicted by upper mantle geodynamic models. *J. Geophys. Res.* (in press) (<http://geodynamics.usc.edu/~becker/bcsb05s.pdf>).
- [19] C.E. Hall, K.M. Fischer, E.M. Parmentier, D.K. Blackman, The influence of plate motions on three-dimensional back arc mantle flow and shear wave splitting, *J. Geophys. Res.* 105 (2000) 28009–28033.
- [20] C. Lithgow-Bertelloni, M.A. Richards, The dynamics of Cenozoic and Mesozoic plate motions, *Rev. Geophys.* 36 (1998) 27–78.
- [21] B. Steinberger, Slabs in the lower mantle—results of dynamic modelling compared with tomographic images and the geoid, *Phys. Earth Planet. Inter.* 118 (2000) 241–257.
- [22] H.-P. Bunge, S.P. Grand, Mesozoic plate-motion history below the northeast Pacific Ocean from seismic images of the subducted Farallon slab, *Nature* 405 (2000) 337–340.
- [23] R. Hartog, S.Y. Schwartz, Subduction-induced strain in the upper mantle east of the Mendocino triple junction, California, *J. Geophys. Res.* 105 (2000) 7909–7930.
- [24] M.K. Savage, Seismic anisotropy and mantle deformation in the western United States and southwestern Canada, *Int. Geol. Rev.* 44 (2002) 913–937.
- [25] S. Chevrot, Multichannel analysis of shear wave splitting, *J. Geophys. Res.* 105 (2000) 21579–21590.
- [26] A. Nicolas, N.I. Christensen, Formation of anisotropy in upper mantle peridotites; a review, in: K. Fuchs, C. Froidevaux (Eds.), *Composition, Structure and Dynamics of the Lithosphere-Asthenosphere System*, . Geodynamics, vol. 16, American Geophysical Union, Washington DC, 1987, pp. 111–123.
- [27] D. Mainprice, G. Barruol, W. Ben Ismail, The seismic anisotropy of the Earth’s mantle: from single crystal to polycrystal, in: S.-I. Karato, A.M. Forte, R.C. Liebermann, G. Masters, L. Stixrude (Eds.), *Earth’s Deep Interior. Mineral Physics and Tomography from the Atomic to the Global Scale*, Geophysical Monograph, vol. 117, American Geophysical Union, Washington DC, 2000, pp. 237–264.
- [28] S.-I. Karato, On the Lehmann discontinuity, *Geophys. Res. Lett.* 51 (1992) 2255–2258.
- [29] K.M. Fischer, D.A. Wiens, The depth distribution of mantle anisotropy beneath the Tonga subduction zone, *Earth Planet. Sci. Lett.* 142 (1996) 253–260.
- [30] J. Wookey, J.-M. Kendall, G. Barruol, Mid-mantle deformation inferred from seismic anisotropy, *Nature* 415 (2002) 777–780.
- [31] E.J. Garnero, V. Maupin, T. Lay, M.J. Fouch, Variable azimuthal anisotropy in Earth’s lowermost mantle, *Science* 306 (2004) 5694.
- [32] G. Hirth, D.L. Kohlstedt, Rheology of the upper mantle and the mantle wedge: a view from the experimentalists, in: J. Eiler (Ed.), *Inside the Subduction Factory*, Geophysical Monograph, vol.

- 138 American Geophysical Union, Washington D.C., 2003, pp. 83–105.
- [33] A. McNamara, S.-I. Karato, P.E. van Keken, Localization of dislocation creep in the lower mantle: implications for the origin of seismic anisotropy, *Earth Planet. Sci. Lett.* 191 (2001) 85–99.
- [34] T.W. Becker, L. Boschi, A comparison of tomographic and geodynamic mantle models, *Geochem. Geophys. Geosyst.* 3 (2002) (2001GC000168).
- [35] T.W. Becker, R.J. O'Connell, Predicting plate velocities with geodynamic models, *Geochem. Geophys. Geosyst.* 2 (2001) (2001GC000171).
- [36] B.H. Hager, R.W. Clayton, Constraints on the structure of mantle convection using seismic observations, flow models, and the geoid, in: W.R. Peltier (Ed.), *Mantle Convection; Plate Tectonics and Global Dynamics, The Fluid Mechanics of Astrophysics and Geophysics*, vol. 4, Gordon and Breach Science Publishers, New York, NY, 1989, pp. 657–763.
- [37] B. Steinberger, Plumes in a convecting mantle: models and observations for individual hotspots, *J. Geophys. Res.* 105 (2000) 11127–11152.
- [38] B.H. Hager, R.J. O'Connell, A simple global model of plate dynamics and mantle convection, *J. Geophys. Res.* 86 (1981) 4843–4867.
- [39] S. Zhong, M.T. Zuber, L. Moresi, M. Gurnis, Role of temperature-dependent viscosity and surface plates in spherical shell models of mantle convection, *J. Geophys. Res.* 105 (2000) 11063–11082.
- [40] D.F. Argus, R.G. Gordon, No-net-rotation model of current plate velocities incorporating plate motion model NUVEL-1, *Geophys. Res. Lett.* 18 (1991) 2039–2042.
- [41] C. Kreemer, W.E. Holt, A.J. Haines, An integrated global model of present-day plate motions and plate boundary deformation, *Geophys. J. Int.* 154 (2003) 5–34.
- [42] G. Soldati, L. Boschi, Whole earth tomographic models: a resolution analysis (abstract), *EOS Trans. AGU* 85 (47) (2004) S13D–S1092D.
- [43] S.P. Grand, R.D. van der Hilst, S. Widiyantoro, Global seismic tomography: a snapshot of convection in the Earth, *GSA Today* 7 (1997) 1–7.
- [44] W. Ben Ismail, D. Mainprice, An olivine fabric database; an overview of upper mantle fabrics and seismic anisotropy, *Tectonophysics* 296 (1998) 145–157.
- [45] H. Jung, S.-I. Karato, Water-induced fabric transitions in olivine, *Science* 293 (2001) 1460–1463.
- [46] H.-R. Wenk, C.N. Tomé, Modeling dynamic recrystallization of olivine aggregates deformed in simple shear, *J. Geophys. Res.* 104 (1999) 25513–25527.
- [47] D.K. Blackman, J.-M. Kendall, Seismic anisotropy of the upper mantle: 2. Predictions for current plate boundary flow models, *Geochem. Geophys. Geosyst.* 3 (2002) (2001GC000247).
- [48] M.J. Fouch, K.M. Fischer, E.M. Parmentier, T.J. M.E. Wyssession, Shear wave splitting, continental keels, and patterns of mantle flow, *J. Geophys. Res.* 105 (2000) 6255–6275.
- [49] C. Gaboret, A.M. Forte, J.-P. Montagner, The unique dynamics of the Pacific Hemisphere mantle and its signature on seismic anisotropy, *Earth Planet. Sci. Lett.* 208 (2003) 219–233.
- [50] M.D. Behn, C.P. Conrad, P.G. Silver, Detection of upper mantle flow associated with the African Superplume, *Earth Planet. Sci. Lett.* 224 (2004) 259–274.
- [51] O. Čadež, Constraints on global mantle-flow models from geophysical data (abstract), In E. Boschi, editor, 9th International Workshop on Numerical Modeling of Mantle Convection and Lithospheric Dynamics, volume 25 of International School of Geophysics, pages 15.16, Erice, Sicily, (2005), Ettore Majorana Foundation and Centre for Scientific Culture.
- [52] É. Kaminski, N.M. Ribe, Time scales for the evolution of seismic anisotropy in mantle flow, *Geochem. Geophys. Geosyst.* 3 (2002) (2001GC000222).
- [53] É. Kaminski, N.M. Ribe, J.T. Browaeys, D-Rex, a program for calculation of seismic anisotropy due to crystal lattice preferred orientation in the convective upper mantle, *Geophys. J. Int.* 157 (2004) 1–9.
- [54] É. Kaminski, The influence of water on the development of lattice preferred orientation in olivine aggregates, *Geophys. Res. Lett.* 29 (2002), doi:10.1029/2002GL014710.
- [55] A. Tommasi, Forward modeling of the development of seismic anisotropy in the upper mantle, *Earth Planet. Sci. Lett.* 160 (1998) 1–13.
- [56] D.K. Blackman, H.-R. Wenk, J.-M. Kendall, Seismic anisotropy of the upper mantle: 1. Factors that affect mineral texture and effective elastic properties, *Geochem. Geophys. Geosyst.* 3 (2002) (2001GC000248).
- [57] E.A. Kneller, P.E. van Keken, S.-I. Karato, J. Park, B-type olivine fabric in the mantle wedge: insights from high-resolution non-Newtonian subduction zone models, *Earth Planet. Sci. Lett.* 237 (2005) 781–797.
- [58] N.M. Ribe, On the relation between seismic anisotropy and finite strain, *J. Geophys. Res.* 97 (1992) 8737–8747.
- [59] L.H. Estey, B.J. Douglas, Upper mantle anisotropy: a preliminary model, *J. Geophys. Res.* 91 (1986) 11393–11406.
- [60] F.D. Stacey, A thermal model of the Earth, *Phys. Earth Planet. Inter.* 15 (1977) 341–348.
- [61] A.M. Dziewoński, D.L. Anderson, Preliminary reference Earth model, *Phys. Earth Planet. Inter.* 25 (1981) 297–356.
- [62] J. Browaeys, S. Chevrot, Decomposition of the elastic tensor and geophysical applications, *Geophys. J. Int.* 159 (2004) 667–678.
- [63] G. Rüpker, A. Tommasi, J.-M. Kendall, Numerical simulations of depth-dependent anisotropy and frequency-dependent wave propagation effects, *J. Geophys. Res.* 104 (1999) 23141–23154.
- [64] R.L. Saltzer, J.B. Gaherty, T.H. Jordan, How are vertical shear wave splitting measurements affected by variations in the orientation of azimuthal anisotropy with depth? *Geophys. J. Int.* 141 (2000) 374–390.
- [65] V. Schulte-Pelkum, D.K. Blackman, A synthesis of seismic *P* and *S* anisotropy, *Geophys. J. Int.* 154 (2003) 166–178.
- [66] B.L.N. Kennett, *Seismic Wave Propagation in Stratified Media*, Cambridge Univ. Press, New York, 1983.
- [67] D.C. Booth, S. Crampin, The anisotropic reflectivity technique: theory, *Geophys. J. R. Astron. Soc.* 72 (1985) 31–45.
- [68] C.H. Chapman, P.M. Shearer, Ray tracing in azimuthally anisotropic media: II. Quasishear wave coupling, *Geophys. J.* 96 (1989) 65–83.
- [69] V. Levin, W. Menke, J. Park, Shear wave splitting in the Appalachians and the Urals: a case for multilayered anisotropy, *J. Geophys. Res.* 104 (1999) 17975–17993.
- [70] W. Menke, V. Levin, The cross-convolution method for interpreting SKS splitting observations, with application to one and two layer anisotropic earth models, *Geophys. J. Int.* 154 (2003) 379–392.
- [71] P.G. Silver, H.H. Chan, Implications for continental structure and evolution from seismic anisotropy, *Nature* 335 (1988) 34–39.

- [72] M.D. Long, R.D. van der Hilst, Estimating shear-wave splitting parameters from broadband recordings in Japan: a comparison of three methods, *Bull. Seismol. Soc. Am.* 95 (2005) 1346–1358.
- [73] D.A. Okaya, T.V. McEvilly, Elastic wave propagation in anisotropic crustal material possessing arbitrary internal tilt, *Geophys. J. Int.* 153 (2003) 344–358.
- [74] S. Chevrot, N. Favier, Komatitsch, Shear wave splitting in three-dimensional anisotropic media, *Geophys. J. Int.* 159 (2004) 711–720.
- [75] S. Chevrot, Finite-frequency vectorial tomography: a new method for high resolution imaging of upper mantle anisotropy, *Geophys. J. Int.* 165 (2) (2006) 641–657 (May).
- [76] M.K. Savage, A.F. Sheehan, Seismic anisotropy and mantle flow from the Great Basin to the Great Plains, western United States, *J. Geophys. Res.* 105 (2000) 13715–13734.
- [77] L.J. Sonder, C.H. Jones, Western United States extension: how the West was widened, *Annu. Rev. Earth Planet. Sci.* 27 (1999) 417–462.
- [78] D. Mainprice, A. Tommasi, H. Couvy, P. Cordier, N.J.J. Frost, Pressure sensitivity of olivine slip systems and seismic anisotropy of Earth's upper mantle, *Nature* 433 (2005) 731–733.
- [79] S. Goes, S. van der Lee, Thermal structure of the North American uppermost mantle inferred from seismic tomography, *J. Geophys. Res.* 107 (2002), doi:10.1029/2000JB000049.
- [80] P. Wessel, W.H.F. Smith, Free software helps map and display data, *EOS Trans. AGU* 72 (1991) 445–446.